

Wannier Functions Dually Localized in Space and Energy

Aaron Mahler

Duke University, Department of Physics, Durham, NC 27708

Jacob Z. Williams

Duke University, Department of Chemistry, Durham, NC 27708

Neil Qiang Su

Department of Chemistry, Key Laboratory of Advanced Energy Materials Chemistry (Ministry of Education) and Renewable Energy Conversion and Storage Center (RECAST), Nankai University, Tianjin 300071, China and Duke University, Department of Chemistry, Durham, NC 27708

Weitao Yang*

Duke University, Department of Chemistry, Durham, NC 27708 and

Duke University, Department of Physics, Durham, NC 27708

(Dated: August 20, 2024)

The construction of Wannier functions from Bloch orbitals offers a unitary freedom that can be exploited to yield Wannier functions with advantageous properties. Minimizing the spatial variance is a well-known choice; another, previously proposed for Wannier functions constructed from the occupied Bloch manifold, minimizes a weighted sum of spatial and energy variance. Departing from all previous work, we carry out the dual localization including both the valence and conduction bands at the same time. We show that this compromised dual localization constructs localized and physically reasonable orbitals from both valence and conduction bands at once. Near the Fermi energy, these dually localized Wannier functions recover bonding and antibonding orbitals for bulk silicon and molecular ethylene, as well as d -orbital character for metallic copper. Because they are both localized and retain information about the orbital energy spectrum, dually localized Wannier functions are well suited to orbital-dependent methods that associate Wannier functions with specific energy ranges.

I. INTRODUCTION

In the single-particle picture of electronic structure theory, the eigenfunctions of the Hamiltonian may be delocalized in space. This is especially true when the Hamiltonian is periodic, $H(\mathbf{r}) = H(\mathbf{r}-\mathbf{R})$, for a set of lattice vectors \mathbf{R} . In this case, the eigenfunctions are Bloch functions $\psi_{\mathbf{k}n}(\mathbf{r}) = e^{i\mathbf{k}\cdot\mathbf{r}}u_{\mathbf{k}n}(\mathbf{r})$, where $u_{\mathbf{k}n}(\mathbf{r})$ shares the periodicity of the Hamiltonian [1]. Bloch functions are indexed by \mathbf{k} , a point in reciprocal space, and a band index corresponding to the n th eigenvalue at that \mathbf{k} -point; that is, $H|\psi_{\mathbf{k}n}\rangle = \varepsilon_{\mathbf{k}n}|\psi_{\mathbf{k}n}\rangle$. Bloch orbitals are completely delocalized in space, as can be seen from the plane wave factor $e^{i\mathbf{k}\cdot\mathbf{r}}$, limiting their utility in describing spatially local properties such as chemical bonds; however, they have a localized energy dispersion $\varepsilon_{\mathbf{k}n}$. Dual to the Bloch orbitals are Wannier functions, which are obtained by a Fourier transform of the Bloch orbitals over the Brillouin zone [2]. They are localized in real space, making them useful for evaluating position-dependent quantities such as the dipole moment [3–5], as a basis set for large-scale simulations [6–9], interpolating band structures [10], as a picture of chemical bonding [11, 12], and as localized orbitals in orbital-dependent methods [13–16].

If N_k \mathbf{k} -points are sampled uniformly from the first Brillouin zone, known as Monkhorst–Pack sampling [17], Wannier functions take the form

$$|w_{\mathbf{R}n}\rangle = \frac{1}{N_k} \sum_{\mathbf{k}} e^{-i\mathbf{k}\cdot\mathbf{R}} |\psi_{\mathbf{k}n}\rangle; \quad (1)$$

\mathbf{R} indexes unit cells in the unfolded supercell, on which the Wannier functions are periodic. Monkhorst–Pack sampling, which we assume throughout the text, yields Wannier functions periodic on an unfolded supercell obeying Born–von Kármán boundary conditions, with the number of primitive unit cells in each real-space lattice direction equal to the number of \mathbf{k} -points sampled in the corresponding reciprocal lattice direction [1]. The Fourier transform normalization convention in Eq. (1) implies the normalization $\langle\psi_{\mathbf{k}n}|\psi_{\mathbf{q}m}\rangle = N_k\delta_{nm}\delta_{\mathbf{k}\mathbf{q}}$, and the inverse transform from Bloch orbital to Wannier function is

$$|\psi_{\mathbf{k}n}\rangle = \sum_{\mathbf{R}} e^{i\mathbf{k}\cdot\mathbf{R}} |w_{\mathbf{R}n}\rangle. \quad (2)$$

Bloch orbitals are defined only up to a global phase at each \mathbf{k} , which leads to a gauge freedom in the construction of the Wannier functions:

$$|w_{\mathbf{R}n}\rangle = \frac{1}{N_k} \sum_{\mathbf{k}} e^{-i\mathbf{k}\cdot\mathbf{R}} e^{i\theta_{\mathbf{k}n}} |\psi_{\mathbf{k}n}\rangle. \quad (3)$$

* weitao.yang@duke.edu

For obtaining localized Wannier functions, a natural choice for this gauge freedom is to choose the phase factors $\theta_n(\mathbf{k})$ such that the Bloch functions $e^{i\theta_{\mathbf{k}n}}|\psi_{\mathbf{k}n}\rangle$ are as smooth as possible in \mathbf{k} . If they are analytic, the resulting Wannier function is exponentially localized [18]. However, multiple bands may cross one another in the Brillouin zone, yielding \mathbf{k} -points with a set of degenerate Bloch functions. Any unitary combination $U^{\mathbf{k}}$ of the degenerate bands remains a set of eigenfunctions of the Hamiltonian. These freedoms lead to *generalized* Wannier functions, which allow the bands to mix by an arbitrary unitary operator $U^{\mathbf{k}}$ at each \mathbf{k} [19]:

$$\begin{aligned} |w_{\mathbf{R}n}\rangle &= \frac{1}{N_k} \sum_{\mathbf{k}} e^{-i\mathbf{k}\cdot\mathbf{R}} \sum_m U_{mn}^{\mathbf{k}} |\psi_{\mathbf{k}m}\rangle \\ &= \frac{1}{N_k} \sum_{\mathbf{k}} e^{-i\mathbf{k}\cdot\mathbf{R}} |\phi_{\mathbf{k}n}\rangle. \end{aligned} \quad (4)$$

We call $|\phi_{\mathbf{k}n}\rangle$ a *transformed* Bloch orbital. Generalized Wannier functions (in the rest of the text, we will simply call them Wannier functions) are thus constructed from a unitary combination of Bloch bands; the combination varies, in general, across the Brillouin zone. For simplicity of notation, we omit the spin index, but our arguments apply independently to each spin channel of a collinear spin-polarized system.

A. Gauge freedom and cost function

The unitary gauges $U^{\mathbf{k}}$ can be chosen to satisfy a desired criterion. In the case of the maximally localized Wannier functions (MLWFs) proposed by Marzari and Vanderbilt [11], they minimize a cost function Ω given by the sum

$$\Omega = \sum_n \langle w_{\mathbf{0}n} | \Delta r^2 | w_{\mathbf{0}n} \rangle \quad (5)$$

of each MLWF's spatial variance

$$\langle w_{\mathbf{0}n} | \Delta r^2 | w_{\mathbf{0}n} \rangle = \langle w_{\mathbf{0}n} | r^2 | w_{\mathbf{0}n} \rangle - |\langle w_{\mathbf{0}n} | \mathbf{r} | w_{\mathbf{0}n} \rangle|^2; \quad (6)$$

the domain of integration is the Born–von Kàrmàn unit cell [1]. Note that Eq. (5) is the natural extension to periodic boundary conditions of Foster-Boys localization for finite systems [20]. Without loss of generality, only the home unit cell $\mathbf{R} = \mathbf{0}$ is included in the cost function because Wannier functions at \mathbf{R} are related by translation to those at $\mathbf{0}$, $w_{\mathbf{R}n}(\mathbf{r}) = w_{\mathbf{0}n}(\mathbf{r} - \mathbf{R})$. Summing over \mathbf{R} would thus change Ω only by a multiplicative constant. The MLWF formulation was originally applied to a *composite* set of Bloch bands, separated by an energy gap from all other states at every point in the Brillouin zone. The gradient of Ω was derived analytically for a composite set by Marzari and Vanderbilt [11], and descent methods are applied to obtain the $U^{\mathbf{k}}$ which minimize Ω . Applied to the occupied orbitals of gapped systems with

vanishing Chern numbers, MLWFs have been proven to be real and exponentially localized in three and fewer dimensions [18, 21–23].

Adding an energy variance term to Ω yields the dual-localization cost function

$$\begin{aligned} F &:= (1 - \gamma)\Omega + \gamma\Xi \\ &= (1 - \gamma) \sum_n \langle w_{\mathbf{0}} | \Delta r^2 | w_{\mathbf{0}n} \rangle \\ &\quad + \gamma \sum_n \langle w_{\mathbf{0}n} | \Delta h^2 | w_{\mathbf{0}n} \rangle. \end{aligned} \quad (7)$$

Here, h is the single-particle Hamiltonian, Ω the spatial spread, and Ξ the energy spread;

$$\langle w_{\mathbf{0}n} | \Delta h^2 | w_{\mathbf{0}n} \rangle = \langle w_{\mathbf{0}n} | h^2 | w_{\mathbf{0}n} \rangle - |\langle w_{\mathbf{0}n} | h | w_{\mathbf{0}n} \rangle|^2 \quad (8)$$

is the energy variance of $|w_{\mathbf{0}n}\rangle$. The mixing term γ can be tuned to prioritize spatial or energy localization (see Sec. II C).

The cost function F was first suggested by Gygi *et al.* [24], and implemented in Giustino and Pasquarello [25] for both electrons and phonons in bulk systems. Our work extends these in two ways. First, [24, 25] apply only to calculations in which the Brillouin zone is sampled only at the origin Γ of reciprocal space. In this case, the transformed Bloch orbitals are equivalent to the Wannier functions; varying the mixing term γ interpolates between MLWFs (at $\gamma = 0$) and Bloch orbitals ($\gamma = 1$), so the resulting $|w_{\mathbf{R}n}\rangle$ are called Wannier–Bloch functions. When $N_k > 1$, a nontrivial discrete Fourier transform is required to map $|\phi_{\mathbf{k}i}\rangle$ to $|w_{\mathbf{R}n}\rangle$, and the Wannier functions do not reduce to the Bloch orbitals at $\gamma = 1$. For this reason, we refer to $|w_{\mathbf{R}n}\rangle$ minimizing F as *dually localized Wannier functions* (DLWFs) in \mathbf{k} -sampled calculations. Second, the DLWFs (or Wannier–Bloch functions) of [24, 25] are constructed only from the manifold of occupied (valence) Bloch bands. We show, however, that F allows Wannier functions to be built from both valence and conduction bands at once, treating both on the same footing; this is discussed more fully in IB.

Molecular orbitals (in open boundary conditions) obtained by minimizing Eq. (7) were used in the localized orbital scaling correction (LOSC) [26], which aims to eliminate delocalization error systematically using localized orbitals [27]. In analogy to wavelets [28], they are called orbitalets, highlighting their compromise of spatial and energy localization. We show that the same cost function, extended to periodic systems with $N_k > 1$, produces physically meaningful localizations when any number of virtual orbitals are included in its domain. We additionally note that similar dual-localization criteria have been proposed in the quantum chemistry literature for vibrational [29] and many-body [30] states.

B. Occupied and unoccupied spaces

The inclusion of energy localization naturally allows for DLWFs to be constructed from both occupied and

unoccupied Bloch orbitals. In principle, a complete basis of functions (with the right periodicity) could be used to generate the DLWFs. We are constrained in practice to starting from a finite number of Bloch orbitals, but—as demonstrated by silicon in Table I—starting from more conduction bands does not change the DLWFs obtained from fewer bands qualitatively. This is a stark contrast to maximally localized Wannier functions. Without the moderating influence of energy localization, MLWFs constructed from more conduction bands become more and more localized in space; in the complete basis set limit, they will tend to a comb of delta functions, no longer physically meaningful orbitals. The dual localization formalism also applies unmodified to metals.

Because we include unoccupied Bloch orbitals, we must consider orbital occupations when considering the projector onto the occupied manifold (that is, the one-particle density matrix):

$$P_{\text{occ}} = \frac{1}{N_k} \sum_{\mathbf{k}n} f_{\mathbf{k}n} |\psi_{\mathbf{k}n}\rangle \langle \psi_{\mathbf{k}n}|, \quad (9)$$

where $f_{\mathbf{k}n} = \langle \psi_{\mathbf{k}n} | P_{\text{occ}} | \psi_{\mathbf{k}n} \rangle$ is the occupation of $|\psi_{\mathbf{k}n}\rangle$ ($f_{\mathbf{k}n} = 0$ or 1 if the system is an insulator). If the DLWFs are constructed solely from the occupied bands ($f_{\mathbf{k}n} = 1$), then also $P_{\text{occ}} = \sum_{\mathbf{k}n} |w_{\mathbf{R}n}\rangle \langle w_{\mathbf{R}n}|$. However, allowing valence and conduction bands to mix means that P_{occ} is no longer diagonal in the Wannier basis:

$$P_{\text{occ}} = \sum_{\mathbf{R}\mathbf{T}mn} \lambda_{\mathbf{R}\mathbf{T}mn} |w_{\mathbf{R}m}\rangle \langle w_{\mathbf{T}n}|, \quad (10)$$

where $\lambda_{\mathbf{R}\mathbf{T}mn} = \langle w_{\mathbf{R}m} | P_{\text{occ}} | w_{\mathbf{T}n} \rangle$ is the pairwise occupation between two Wannier functions. The matrix ($\lambda_{\mathbf{R}\mathbf{T}mn}$) is Hermitian, and while the effective occupation $\lambda_{\mathbf{R}\mathbf{R}nn}$ of $|w_{\mathbf{R}n}\rangle$ is not in general an integer, it does satisfy $0 \leq \lambda_{\mathbf{R}\mathbf{R}nn} \leq 1$.

We can also write P_{occ} in the basis of transformed Bloch orbitals as

$$\begin{aligned} P_{\text{occ}} &= \frac{1}{N_k^2} \sum_{\mathbf{k}m} \sum_{\mathbf{q}n} \langle \phi_{\mathbf{k}m} | P_{\text{occ}} | \phi_{\mathbf{q}n} \rangle |\phi_{\mathbf{k}m}\rangle \langle \phi_{\mathbf{q}n}| \\ &= \frac{1}{N_k} \sum_{\mathbf{k}mn} \lambda_{\mathbf{k}mn} |\phi_{\mathbf{k}m}\rangle \langle \phi_{\mathbf{q}n}|, \end{aligned} \quad (11)$$

where $|\phi_{\mathbf{k}n}\rangle = \sum_m U_{mn}^{\mathbf{k}} |\psi_{\mathbf{k}m}\rangle$. The pairwise occupation $\lambda_{\mathbf{k}mn}$ between $|\phi_{\mathbf{k}m}\rangle$ and $|\phi_{\mathbf{k}n}\rangle$ is not diagonal in the band index n if valence and conduction bands are mixed by $U^{\mathbf{k}}$, although it does remain diagonal in \mathbf{k} ; as in the Wannier basis, $0 \leq \lambda_{\mathbf{k}nn} \leq 1$.

The local occupation matrices ($\lambda_{\mathbf{k}mn}$) and ($\lambda_{\mathbf{R}\mathbf{T}mn}$) are related by discrete Fourier transforms; and their traces, restricted to a single \mathbf{k} point (or unit cell \mathbf{R}), give the number of electrons below the Fermi energy at \mathbf{k} (in the unit cell \mathbf{R}). That is,

$$\text{Tr}_{\mathbf{k}} (\lambda_{\mathbf{k}mn}) = \sum_n \lambda_{\mathbf{k}nn} = N_{\text{occ}}(\mathbf{k}), \quad (12)$$

and

$$\text{Tr}_{\mathbf{R}} (\lambda_{\mathbf{R}\mathbf{T}mn}) = \sum_n \lambda_{\mathbf{R}\mathbf{R}nn} = \frac{1}{N_k} \sum_{\mathbf{k}} N_{\text{occ}}(\mathbf{k}). \quad (13)$$

II. METHODS

The procedure outlined by Marzari and Vanderbilt in [11] minimizes Ω for a composite set of energy bands by determining its gradient with respect to the gauge unitaries $U^{\mathbf{k}}$. This is accomplished by splitting the cost function into two positive definite quantities, $\Omega = \Omega_{\text{I}} + \tilde{\Omega}$. Ω_{I} is invariant to the choice of gauge, so minimizing Ω is equivalent to minimizing only the gauge-dependent term $\tilde{\Omega}$. For a set of N_w Wannier functions,

$$\Omega_{\text{I}} = \sum_n^{N_w} \left(\langle w_{\mathbf{0}n} | r^2 | w_{\mathbf{0}n} \rangle - \sum_m^{N_w} \sum_{\mathbf{R}}^{N_k} |\langle w_{\mathbf{R}m} | \mathbf{r} | w_{\mathbf{0}n} \rangle|^2 \right), \quad (14)$$

and the gauge-dependent spatial cost is

$$\begin{aligned} \tilde{\Omega} &= \sum_{m \neq n}^{N_w} \sum_{\mathbf{R}}^{N_k} |\langle w_{\mathbf{R}m} | \mathbf{r} | w_{\mathbf{0}n} \rangle|^2 \\ &\quad + \sum_n^{N_w} \sum_{\mathbf{R} \neq \mathbf{0}}^{N_k} |\langle w_{\mathbf{R}n} | \mathbf{r} | w_{\mathbf{0}n} \rangle|^2. \end{aligned} \quad (15)$$

By an argument exactly analogous to that in [11],

$$\begin{aligned} \Xi &= \Xi_{\text{I}} + \tilde{\Xi} \\ &= \sum_n \left(\langle w_{\mathbf{0}n} | h^2 | w_{\mathbf{0}n} \rangle - \sum_{\mathbf{R}m} |\langle w_{\mathbf{R}m} | h | w_{\mathbf{0}n} \rangle|^2 \right) \\ &\quad + \sum_n \sum_{\mathbf{R}m \neq \mathbf{0}n} |\langle w_{\mathbf{R}m} | h | w_{\mathbf{0}n} \rangle|^2, \end{aligned} \quad (16)$$

where Ξ_{I} is gauge-invariant. Thus, for a composite set of bands, we could find the unitary operators $U^{\mathbf{k}}$ that define the DLWF gauge by minimizing

$$\tilde{F} = (1 - \gamma)\tilde{\Omega} + \gamma\tilde{\Xi}. \quad (17)$$

Because differentiation is linear, the gradients of $\tilde{\Omega}$ and $\tilde{\Xi}$ with respect to $U^{\mathbf{k}}$ can be found in parallel, and the minimum found with an iterative procedure. However, virtual Bloch bands almost never form a composite set, and we require an additional step to construct DLWFs.

A. Disentanglement

The valence bands of metals, and the conduction bands of most systems, cannot be separated from the rest of the

bands by an energy gap everywhere in the Brillouin zone; such bands are said to be *entangled*. Souza et al. developed a *disentanglement* method, extracting a subset of interest from a set of entangled bands [10]. From N_b Bloch bands, disentanglement obtains $N_w \leq N_b$ composite bands that minimize Ω_I by an iterative process. We write the disentangled bands as $|\tilde{\psi}_{\mathbf{k}i}\rangle$; they retain the same index \mathbf{k} as the original Bloch functions, but have a new band index i running from 1 to N_w . They are calculated from the Bloch orbitals by

$$|\tilde{\psi}_{\mathbf{k}i}\rangle = \sum_n V_{in}^{\mathbf{k}} |\psi_{\mathbf{k}n}\rangle, \quad (18)$$

where $V^{\mathbf{k}}$ is a $N_w \times N_b$ semiunitary transformation that satisfies $V^{\mathbf{k}}(V^{\mathbf{k}})^\dagger = \mathbb{1}$, the N_w -dimensional identity operator. These disentangled bands form the smoothest possible N_w -dimensional subspace given the original N_b bands; they are then used as the input for N_w transformed Bloch orbitals $|\phi_{\mathbf{k}i}\rangle$, which finally become the Wannier functions $|w_{\mathbf{R}i}\rangle$. Altogether, the procedure of disentanglement, localization, and Wannierization can be written as

$$\begin{aligned} w_{\mathbf{R}i}(\mathbf{r}) &= \frac{1}{N_k} \sum_{\mathbf{k}} e^{-i\mathbf{k}\cdot\mathbf{R}} \phi_{\mathbf{k}i}(\mathbf{r}) \\ &= \frac{1}{N_k} \sum_{\mathbf{k}} e^{-i\mathbf{k}\cdot\mathbf{R}} \sum_j U_{ij}^{\mathbf{k}} \tilde{\psi}_{\mathbf{k}j}(\mathbf{r}) \\ &= \frac{1}{N_k} \sum_{\mathbf{k}} e^{-i\mathbf{k}\cdot\mathbf{R}} \sum_j U_{ij}^{\mathbf{k}} \sum_n V_{jn}^{\mathbf{k}} \psi_{\mathbf{k}n}(\mathbf{r}). \end{aligned} \quad (19)$$

In principle, we could modify the disentanglement procedure in the same way that F modifies Ω , finding the N_w -dimensional subspace that minimizes

$$F_I = (1 - \gamma)\Omega_I + \gamma\Xi_I. \quad (20)$$

In practice, however, we find this unnecessary and use the space-only disentanglement of [10] as the first step in computing the DLWFs. In particular, this procedure projects the Hamiltonian onto the subspace spanned by $\{|\tilde{\psi}_{\mathbf{k}i}\rangle\}$ after each iteration, yielding a so-called disentangled Hamiltonian $\tilde{h} = \sum_{\mathbf{k}} V^{\mathbf{k}} h (V^{\mathbf{k}})^\dagger$ that satisfies

$$\langle \tilde{\psi}_{\mathbf{k}i} | \tilde{h} | \tilde{\psi}_{\mathbf{q}j} \rangle = N_k \delta_{\mathbf{k}\mathbf{q}} \delta_{ij} \tilde{\varepsilon}_{\mathbf{k}i} \quad (21)$$

where $\tilde{\varepsilon}_{\mathbf{k}i}$ is a disentangled energy eigenvalue. If we use the disentangled Hamiltonian is used in Ξ , then $\Xi_I = 0$. (See the Supplemental Material for the derivation.)

The difference between the disentangled Hamiltonian \tilde{h} and the full Hamiltonian depends on the subspace projectors $V^{\mathbf{k}}$. If every disentangled eigenvalue $\tilde{\varepsilon}_{\mathbf{k}i}$ corresponds exactly to a Bloch eigenvalue $\varepsilon_{\mathbf{k}n}$ at the same \mathbf{k} -point, then h and \tilde{h} commute inside the disentangled subspace and using \tilde{h} is equivalent to using h in Ξ . We do not quite achieve this in practice, but the existing disentanglement procedure creates a band structure nearly

equivalent to the full band structure except for high-energy conduction bands. We can thus reproduce the band structure around the Fermi energy accurately by including sufficiently many unoccupied orbitals before disentanglement; the band structure interpolated from the resulting Wannier functions differs appreciably from the original only well above the Fermi energy. For example, a band structure for silicon disentangling 34 bands to 30 yields DLWFs that interpolate a qualitatively accurate band structure up to 20 eV above the Fermi energy (Fig. 1).

Replacing the full Hamiltonian h by \tilde{h} also means that $\sum_i \langle w_{\mathbf{0}i} | \tilde{h}^2 | w_{\mathbf{0}i} \rangle$ is gauge-invariant, since

$$\sum_n \langle w_{\mathbf{0}n} | \tilde{h}^2 | w_{\mathbf{0}n} \rangle = \frac{1}{N_k} \text{Tr} \left[(\tilde{h})^2 \right]. \quad (22)$$

We thus decompose

$$\begin{aligned} \Xi &= \sum_i \left[\langle w_{\mathbf{0}i} | \tilde{h}^2 | w_{\mathbf{0}i} \rangle - |\langle w_{\mathbf{0}i} | \tilde{h} | w_{\mathbf{0}i} \rangle|^2 \right] \\ &:= \Xi_{\text{SA}} - \Xi_{\text{AS}}, \end{aligned} \quad (23)$$

where the squared average energy term Ξ_{SA} is invariant to the choice of Wannier basis. As is true for Ω in Γ -sampled systems, minimizing Ξ (or $\tilde{\Xi}$) is equivalent to maximizing the average energy squared term Ξ_{AS} .

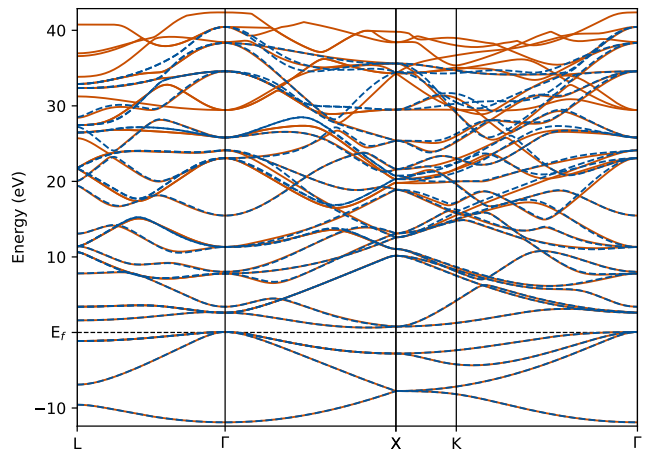


FIG. 1. PBE band structure of silicon (valence band maximum set to zero), disentangling 34 bands to 30 Wannier functions, with disentangled states below the Fermi energy fixed to reproduce the Bloch bands exactly. Solid orange bands are non-self-consistently computed in **Quantum ESPRESSO**; dashed blue bands are interpolated from the DLWFs. Mixing parameter $\gamma = 0.01$.

B. Energy cost gradient

We now derive the gradient of Ξ_{AS} with respect to the localization unitary $U^{\mathbf{k}}$. To first order, $U^{\mathbf{k}}$ can be written

as a small anti-Hermitian perturbation to the identity; $U^{\mathbf{k}} \approx \mathbb{1} + W^{\mathbf{k}}$, with $(W^{\mathbf{k}})^\dagger = -W^{\mathbf{k}}$. Then $\partial \Xi_{\text{AS}} / \partial U^{\mathbf{k}}$ is obtained via the matrix calculus identity

$$\frac{d \text{Re Tr} [MW]}{dW} = \frac{1}{2} (M - M^\dagger) := \mathcal{A}[M]. \quad (24)$$

To see why this is useful, observe that we may write

$$\begin{aligned} \Xi_{\text{AS}} &= \sum_i \left| \langle w_{\mathbf{0}i} | \tilde{h} | w_{\mathbf{0}i} \rangle \right|^2 \\ &= \sum_i \left| \frac{1}{N_k} \sum_{\mathbf{k}j} |U_{ij}^{\mathbf{k}}|^2 \tilde{\epsilon}_{\mathbf{k}j} \right|^2 \\ &= \sum_i \left| \frac{1}{N_k} \sum_{\mathbf{k}} B_{ii}^{\mathbf{k}} \right|^2, \end{aligned} \quad (25)$$

where $B_{ij}^{\mathbf{k}} = (U^{\mathbf{k}} \tilde{h} (U^{\mathbf{k}})^\dagger)_{ij}$ is the Hamiltonian in the transformed Bloch basis. The change in Ξ_{AS} to first order in $W^{\mathbf{k}}$ is then

$$\begin{aligned} d\Xi_{\text{AS}} &= \frac{4}{N_k^2} \sum_i \left(\sum_{\mathbf{k}} \text{Re} (B^{\mathbf{k}} W^{\mathbf{k}})_{ii} \right) \left(\sum_{\mathbf{k}'} B_{ii}^{\mathbf{k}'} \right) \\ &= \frac{4}{N_k^2} \sum_{\mathbf{k}\mathbf{k}'} \text{Re Tr} [C^{(\mathbf{k},\mathbf{k}')} W^{\mathbf{k}}], \end{aligned} \quad (26)$$

where $(C^{(\mathbf{k},\mathbf{k}')})_{ij} = B_{ji}^{\mathbf{k}} B_{jj}^{\mathbf{k}'}$. We can thus write the gradient in terms of the superoperator \mathcal{A} , defined in Eq. (24), as

$$\begin{aligned} \frac{d\Xi_{\text{AS}}}{dW^{\mathbf{k}}} &= \frac{4}{N_k} \sum_{\mathbf{k}'} \mathcal{A} [C^{(\mathbf{k},\mathbf{k}')}] \\ &= \frac{2}{N_k} \sum_{\mathbf{k}'} [C^{(\mathbf{k},\mathbf{k}')} - (C^{(\mathbf{k},\mathbf{k}')})^\dagger]. \end{aligned} \quad (27)$$

In this form, it appears the gradient \mathbf{k} -point depends on every other \mathbf{k} -point in the Brillouin zone. However, we can sum $C^{(\mathbf{k},\mathbf{k}')}$ over \mathbf{k}' prior to evaluating the gradient. Thus

$$\left[\frac{d\Xi_{\text{AS}}}{dW^{\mathbf{k}}} \right]_{ij} = 2B_{ij}^{\mathbf{k}} (\bar{E}_j - \bar{E}_i), \quad (28)$$

where $\bar{E}_j = \langle w_{\mathbf{0}j} | \tilde{h} | w_{\mathbf{0}j} \rangle$ is the average energy of a Wannier function (with respect to the disentangled Hamiltonian). In essence, these terms penalize the mixing of Bloch orbitals proportionally to the difference in average energy of the Wannier functions they are used to construct. This form also makes clear that the computational cost of computing $d\Xi_{\text{AS}}/dW^{\mathbf{k}}$ is independent of N_k ; the cost of energy localization is linear in N_k .

C. Mixing parameter

We now remark on the mixing parameter γ introduced in Eq. (7). Setting $\gamma = 0$ recovers the MLWF cost function Ω . Setting $\gamma = 1$ returns the Bloch orbitals if the

Brillouin zone is sampled only at Γ . However, when $N_k > 1$, setting $\gamma = 1$ yields transformed Bloch orbitals that are simply the Bloch orbitals ordered by their energy at each \mathbf{k} -point. When there are band crossings in the Brillouin zone, the energy-ordered Bloch orbitals will not be smooth in \mathbf{k} , giving poor spatial localization. Choosing γ strictly between 0 and 1 provides Wannier functions localized in both space and energy.

In a related work for molecules, this cost function was used in an orbital-dependent density functional method called the localized orbital scaling correction (LOSC) [26]. In that work, γ was chosen to minimize the error in several experimentally realizable quantities in a test suite of molecules. In Å and eV, the units of space and energy used in `wannier90`, this value is $\gamma = 0.47714$. For details on this value in relation to the value published in [26], see the Supplemental Material. At $\gamma = 0.47714$, we find that Bloch orbitals mix substantially in the construction of DLWFs at a given \mathbf{k} -point when the difference in their energies is less than about 2 eV. This natural penalty to mixing of orbitals widely separated in energy means that the dual localization procedure yields converged frontier orbitals irrespective of the number of high-energy virtual states included.

D. Computational details

Following Marzari and Vanderbilt [11] for Ω and the previous section for Ξ , we compute $\partial F / \partial U^{\mathbf{k}}$ at each \mathbf{k} -point. Given an initial guess or disentanglement, either a conjugate gradient or steepest descent algorithm is used to minimize F . We implement the DLWF localization in a locally maintained fork of the open-source `wannier90` code [31–33]. Some modifications to the descent algorithm were required for Ξ . The steepest descent portion of the algorithm was left unchanged, but we found that the step size that produced the best localization was system-dependent. To account for this, we sweep a range of step sizes in order to obtain the best minimum for each localization. For steps when the conjugate-gradient descent and parabolic line search were used, we found that the Polak–Ribiere coefficient [34] sometimes provides better convergence than the default Fletcher–Reeves coefficient [35, 36].

Because we allow the inclusion of unoccupied orbitals, we also use the disentanglement procedure on the highest-energy conduction bands considered for localization [10]. When including virtual bands, the choice of how many bands and DLWFs to include is increased until the orbitals of interest, typically the ones around the Fermi energy, are converged. Convergence of high-lying virtual bands was found to be difficult; to sidestep this issue, we implement a program option allowing the exclusion of specified bands from the cost function convergence criterion. We consider the DLWFs converged if their cost from Eq. (7) does not appreciably change with the addition of more unoccupied bands. The modified version of

the code may be found at [37]; more details on the functionality added to `wannier90` are in the Supplemental Material.

III. RESULTS

We obtain Bloch functions using the PBE density functional [38] in the plane-wave basis, using optimized norm-conserving Vanderbilt pseudopotentials [39] from the PseudoDojo [40]; calculations are performed using the open-source Quantum ESPRESSO code suite [41, 42]. The Brillouin zone is always sampled with Monkhorst-Pack meshes [17] centered at Γ , the origin of reciprocal space. For silicon and ethylene, we use a wave function kinetic energy cutoff $E_{\text{cut}} = 60$ Ry; for copper, we set $E_{\text{cut}} = 100$ Ry. In all cases, E_{cut} for the density is four times that used for the wave functions. As mentioned in Section II, we use a modified version of the `wannier90` code [31–33] to obtain the DLWFs. We set the space-energy mixing parameter $\gamma = 0.47714$ unless stated otherwise. Since the DLWFs are not always real, isoplots are of the DLWF densities, $|w_{0n}(\mathbf{r})|^2$, rather than of the DLWFs themselves. All lengths are reported in \AA and all energies in eV.

A. Silicon

First we consider the well-studied semiconductor silicon in the diamond lattice. For the self-consistent calculation we use an $8 \times 8 \times 8$ \mathbf{k} -mesh; for computational efficiency, we use a $4 \times 4 \times 4$ \mathbf{k} -mesh for obtaining virtual Bloch orbitals and localization. We use the experimental lattice parameter $a = 5.431 \text{ \AA}$ [43]. The gap of Si is small, 0.71 eV in our PBE calculation. It is indirect, however; the smallest direct gap in the Brillouin zone is 2.56 eV, at Γ .

TABLE I. Energy degeneracies of DLWFs ordered from lowest to highest for the occupied, frontier, and converged calculations for silicon. All three calculations have the same degeneracy patterns up to their highest energy when ordered by energy, which allows them all to share the first column. We say two or more DLWFs are degenerate if they fall within a 0.2 eV energy window and the energy reported in the second to fourth columns is the average of all DLWFs in an energy window. Full energy spectra can be found in the Supplemental Material.

Degeneracy	Occupied	Frontier	Converged
1	-3.22898	-3.234109	-3.234141
1	0.53392	0.52817	0.528461
2	3.71853	3.7333	3.738822
4		11.4122	10.63073
2			15.69691

1. Occupied states

Constructing DLWFs from only the occupied bands of silicon yields Wannier functions which are not degenerate in energy and have different shapes; this contrasts with the MLWF procedure, which yields four degenerate Wannier functions related by space-group symmetry operations. The lowest-energy DLWF is tetrahedral, while the two highest-energy orbitals are degenerate, each having three lobes centered along a Si–Si bond; the energy degeneracy pattern of the DLWFs is shown in Table I. The MLWFs, on the other hand, are fourfold degenerate in energy and have tight-binding character, with a single lobe centered along a bond.

2. Frontier states

We expect the valence bands of semiconductors to yield degenerate MLWFs that approximate bonding molecular orbitals; localizing the same number of low-lying conduction bands with the MLWF procedure often yields degenerate functions of antibonding character. Since the conduction states are entangled with higher-energy bands, Souza *et al.* [10] disentangled 12 bands down to 8 when investigating silicon. Here, we use the same disentanglement with a frozen disentanglement window at the Fermi energy, 6.23 eV. Using Eq. (7) for the cost function on this subspace, we obtain occupied orbitals very similar to those found in Sec. III A 1 above, as can be seen from their shared degeneracy pattern (Table I). The conduction orbitals, however, form a fourfold degenerate anti-bonding set, qualitatively equivalent to MLWFs constructed from the four lowest-lying conduction bands.

We also use this system to explore the effects of varying values of γ in the cost function. Allowing both valence and conduction bands to mix in the MLWF construction yields eight Wannier functions degenerate in energy. As we increase γ , we observe WFs more closely associated with specific energy ranges and stepwise lifting of degeneracy (see Fig. 2a), but spatial localization is suppressed at the same time (see Fig. 2b).

In order to show how the mixing parameter γ affects band interpolation along a \mathbf{k} -path, we calculate the difference between the interpolated eigenvalues $\tilde{\varepsilon}_{\mathbf{k}i}$ and those ($\varepsilon_{\mathbf{k}n}$) obtained before disentanglement; the results are shown in Fig. 3. (Note that the low-energy disentangled bands i of gapped systems can be reliably identified one-to-one with original bands n_i .) We calculate the mean squared error per band as

$$\bar{\Delta} = \frac{1}{N_w} \sum_i \left[\frac{1}{N_k} \sum_{\mathbf{k}} (\varepsilon_{\mathbf{k}n_i} - \tilde{\varepsilon}_{\mathbf{k}i})^2 \right]; \quad (29)$$

here, the $\sum_{\mathbf{k}}$ is over the band structure path, not a Monkhorst–Pack mesh. The interpolation error in Fig. 3 at $\gamma = 0$ arises primarily from the virtual orbitals; that is, from disentanglement rather than interpolation. The

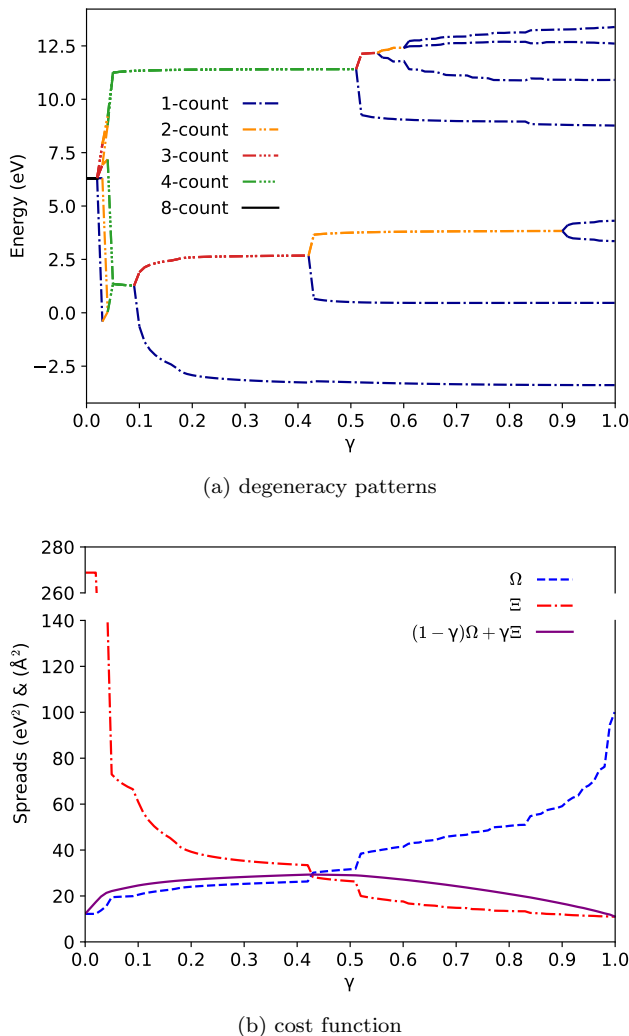


FIG. 2. (a) Degeneracy patterns of the average energy $\langle \tilde{h} \rangle$ of the DLWFs in silicon against γ from Eq. (7). The color and line type indicate the degeneracy of the DLWFs; we call $|w_m\rangle$ and $|w_n\rangle$ degenerate if $|\langle \tilde{h} \rangle_n - \langle \tilde{h} \rangle_m| < 0.2 \text{ eV}$. At $\gamma = 0$ (MLWFs), we obtain degenerate sp^3 hybrid orbitals, with each MLWF having occupancy $\lambda_{nn} = 0.5$ and $\langle h \rangle = 6.3 \text{ eV}$. In the range $0.02 < \gamma < 0.05$, the DLWF degeneracy pattern rapidly changes before splitting into two degenerate sets between $0.05 \leq \gamma \leq 0.09$: the occupied and unoccupied orbitals. The degeneracy of unoccupied DLWFs is lifted at $\gamma = 0.53$, while the first lifting of degeneracy for occupied DLWFs occurs at $\gamma = 0.1$. (b) Spatial cost Ω , energy cost Ξ , and total cost F against γ in Eq. (7). Since the total cost is a convex sum of Ω and Ξ , it always remains between their two values. The sharp changes in Ω and Ξ correspond to degeneracy splitting in (a). Note the discontinuity in the vertical axis.

noticeable upticks in interpolation error for the valence states around $\gamma = 0.4$ and for the conduction states around $\gamma = 0.5$ are due to groups of degenerate Wannier functions splitting into separate states (Fig. 2a). This splitting of degeneracy is due to the energy cost term becoming larger than the spatial cost term for a given

DLWF configuration. For a given set of DLWFs, then, lower-degeneracy DLWFs always have a larger spatial spread than their higher-degeneracy counterparts. The larger spatial spread of these lower-degeneracy DLWFs yields a poorer interpolation of the band structure because Wannier function interpolation accuracy relies on rapid spatial decay of the Wannier functions. A comparison of interpolated band structure plots at some specific values of γ is provided in the Supplemental Material.

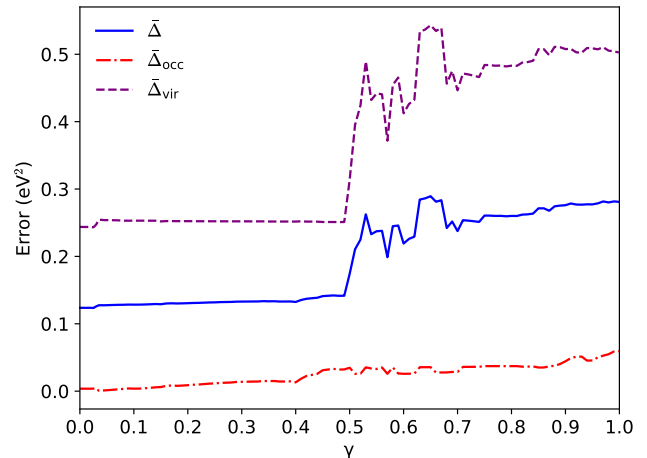


FIG. 3. Band average interpolation error using Eq. (29) along the \mathbf{k} -path used in Fig. 1 (L- Γ -X-K-L) for the frontier states of silicon. The solid line (blue) averages all 8 frontier states, the dash-dotted line (red) is for the 4 highest valence bands, and the dashed line (purple) is for the 4 lowest conduction bands. (Color online.)

3. Converged frontier states

Next, we show convergence results when higher-energy virtual bands are included. For this result, we find that the spatial variance of the highest-energy occupied DLWF is well converged when 34 bands are disentangled to 30. Notably, we find that the shapes of the resulting DLWFs are qualitatively the same as those found when including only occupied orbitals (frontier orbitals), as in Sec III A 1 (Sec III A 2), which can be seen from their shared degeneracy patterns in Table I. We note, however, that the spatial variance Δr^2 of the lowest unoccupied DLWFs is larger than when only four unoccupied bands are included. This is due to the fact that the disentanglement in the latter case directly modifies the conduction bands, smoothing them in \mathbf{k} -space and increasing the localization of the resulting Wannier functions. Including more virtual orbitals in the localization procedure means that disentanglement smooths only the high-energy conduction bands, removing this effect. For isosurface plots of the eight lowest-energy DLWF densities, see Fig. 4. For more data on individual DLWFs, see the Supplemental Material.

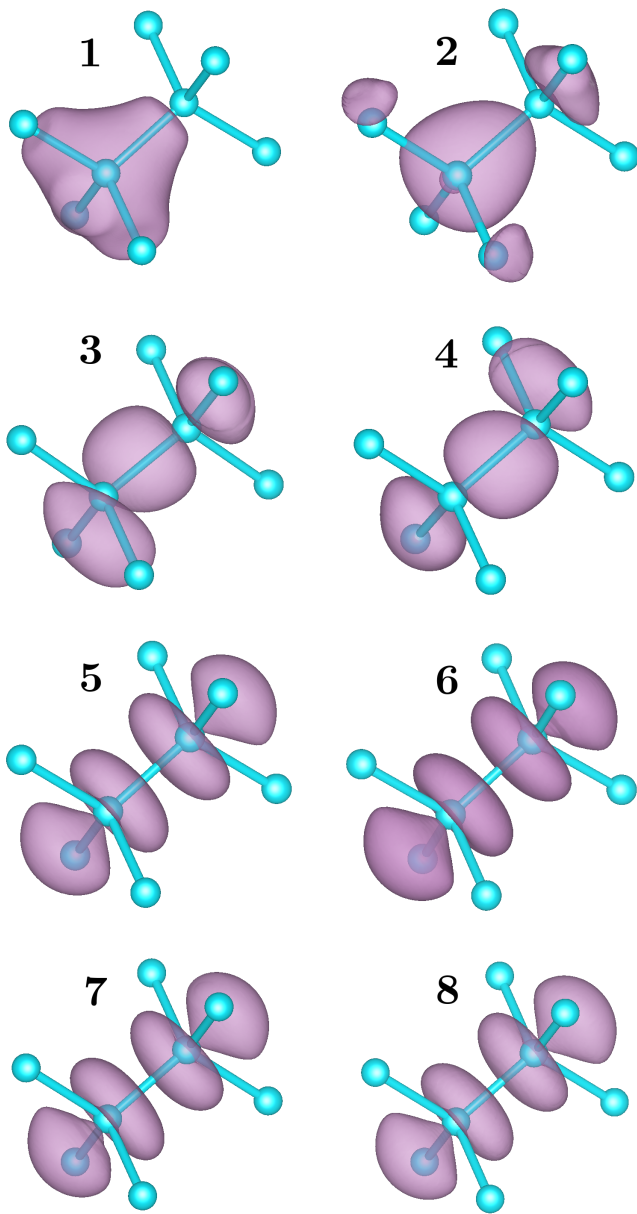


FIG. 4. DLWF density isoplots for silicon (isovalue 0.6) using $\gamma = 0.47714$. They are labeled in ascending order of DLWF average energy starting at the lowest energy. Note that even though this is the result of using 30 disentangled Bloch orbitals per \mathbf{k} -point for construction, the degeneracy pattern is the same as the frontier-only case show in Fig. 2a for the value of $\gamma = 0.47714$.

B. Copper

We next investigate copper in a face-centered cubic lattice, with the experimental lattice parameter $a = 3.614 \text{ \AA}$ [44]. For the self-consistent calculation, we use a $16 \times 16 \times 16$ \mathbf{k} -mesh; for the virtual states and localization, we use $10 \times 10 \times 10$ \mathbf{k} -points. Since the unoccupied bands of copper are very steep and energy localization re-

stricts the mixing of bands far apart in energy, we do not require many bands above the Fermi level. Noting that there are 9.5 electrons per spin channel, we disentangle 23 bands to 17 Wannier functions, with frozen disentanglement required below 40 eV, well above the Fermi energy (17.04 eV). This results in a set of disentangled bands that only differs from the parent DFA at the top of the energy window. Using the $\gamma = 0.47714$, we find that the fully occupied orbitals self-organize into pure s , p , and d -type DLWFs (see Fig. 5). The partially occupied DLWF associated with the frontier band has d -type character, but is delocalized across multiple atoms. Information on individual DLWFs is provided in the Supplemental Material.

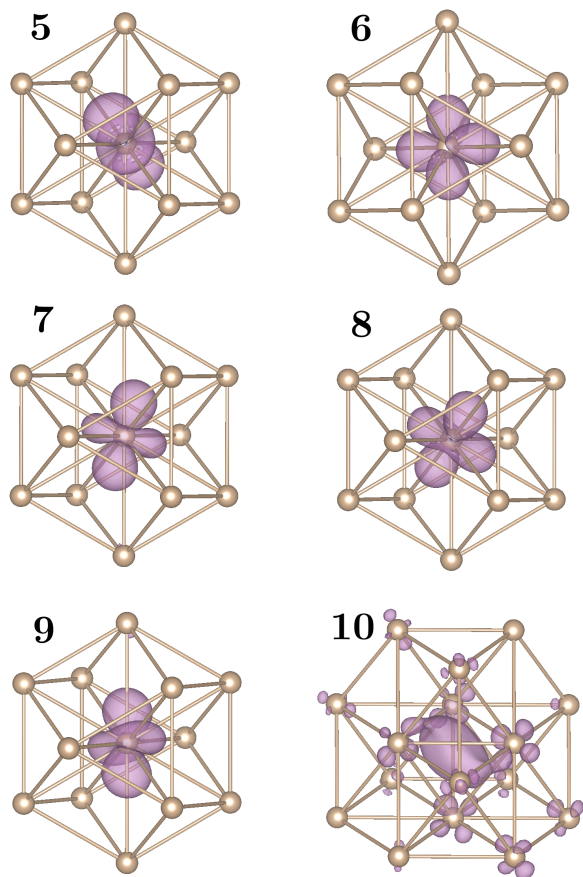


FIG. 5. DLWF density isoplots of copper at isovalue 0.6 using $\gamma = 0.47714$. These are the six highest-energy occupied DLWFs labeled in ascending order of average energy, starting with the fifth-lowest energy. The four DLWFs of lowest energy (not shown) correspond to the occupied $3s$ and $3p$ states. DLWF 10 is only partially occupied, as it is comprised mostly of the frontier Bloch band. More atoms are shown for the isplot of DLWF 10 due to its delocalized nature.

C. Ethylene

To demonstrate the utility of dual localization in molecules, we simulate ethylene with the geometry from [11]. We use a 10 Å unit cell with the molecule centered at the origin and sample only $\mathbf{k} = \Gamma$. Thus, disentangling is unnecessary, and we construct 36 DLWFs from 36 bands, 6 of which are occupied. Setting $\gamma = 0.47714$ recovers DLWFs closely related to molecular orbitals. The lowest-energy DLWF corresponds to a σ bond between the carbon atoms, and the next four resemble combinations of C–C and C–H bonding orbitals. The highest-energy occupied DLWF corresponds to a π bonding orbital, and the lowest unoccupied DLWF to a π^* antibonding orbital (Fig. 6). The four unoccupied DLWFs next lowest in energy are degenerate, as noted in the tabulated DLWF information provided in the Supplemental Material, and can be characterized as C–H σ^* orbitals.

IV. DISCUSSION

We have shown that including energy localization in the construction of Wannier functions results in DLWFs localized both in space and in energy. This allows for bands widely separated in energy to be included in the Wannier function construction without allowing the mixing of bands far apart in energy; furthermore, the localization procedure naturally produces orbitals associated with certain energies, organizing itself along the Hamiltonian’s spectrum. DLWFs with occupation close to 1 also retain the behavior seen in MLWFs, appearing as tight-binding or atomic orbitals and retaining the symmetry of the underlying system. Using the LOSC cost function, $\gamma = 0.47714$, the DLWFs recover atomic states such as the d orbitals of copper (Fig. 5). In diamond-lattice silicon, the DLWFs separate naturally into occupied and unoccupied manifolds. We also find that the occupied atom-centered Wannier function (labeled 1 in Fig. 4) is much more localized than the other bond-centered DLWFs. This agrees with Kohn [45], which found that atom-centered Wannier functions produce a more localized state than their bond-centered counterparts. The Supplemental Material includes tables with the individual occupation numbers and spatial spreads of all DLWFs mentioned here.

The LOSC cost function can also recover molecular orbitals such as the σ and π bonding orbitals in ethylene (Fig. 6). This shows that DLWFs have the potential to produce chemically relevant frontier orbitals automatically, with no need for manually enforced energy cutoffs or for separating the occupied and unoccupied spaces.

The fact that DLWFs offer a frontier orbital description localized in space means that they can be employed for orbital-dependent DFT methods [13–16, 26]. Many of these methods attempt to correct the well-known failure of density functional approximations to give energy piecewise linear in fractional occupation [46]. In order to

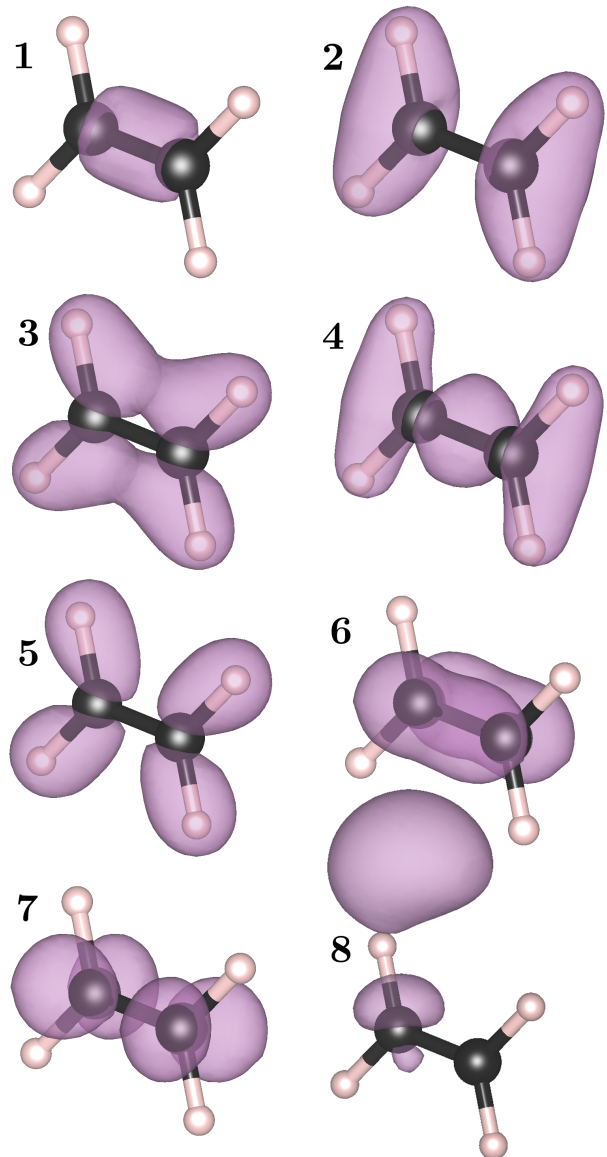


FIG. 6. DLWF density isoplots for ethylene using $\gamma = 0.47714$. Isovalues: 160 (DLWF 1), 60 (DLWFs 2–7), 30 (DLWF 8). The isosurface between DLWF 6 and DLWF 8 belongs to DLWF 8.

correct this nonlinearity, many such corrections invoke localized frontier orbitals; a popular choice is to use MLWFs constructed from the highest-energy composite set of occupied Bloch bands. The fractional occupations in DLWFs play an important role in the LOSC correction to density functional approximations [26, 27]. As DLWFs are naturally associated with an energy level, they offer a localized charge description of frontier orbitals for both the occupied and the unoccupied spaces. Thus, they can describe both occupied and unoccupied frontier orbitals with the favorable symmetry characteristics of Wannier functions but without having to compute each separately

or arbitrarily limit the number of conduction states.

When the Wannier function construction includes entangled bands, Damle and Lin [47] have questioned whether sequential disentanglement and localization can find the globally optimal solution as separate procedures, and proposed a unified localization method offering a possible solution to this problem. For a composite set of bands, this method reduces to the selected columns of the density matrix method [48, 49]; in that case, as with the original MLWF construction, energy cutoffs can be enforced explicitly to limit the energy spread of the Wannier functions. However, because the unified method of Damle and coworkers relies on the exponential decay of off-diagonal elements of the one-particle density matrix in space, it is unclear whether it can be adapted to include energy localization in the construction of the Wannier functions while allowing the inclusion of Bloch orbitals widely separated in energy, as shown in this work.

Finally, we comment on the (lack of) reality of the DLWFs. Marzari and Vanderbilt [11] conjectured that maximally localized Wannier functions ($\gamma = 0$) are purely real (up to a global phase). The conjecture was proven true in [22] for Wannier functions constructed by minimizing any

functional symmetric under time reversal, provided that the optimum is unique. Our cost function F obeys time-reversal symmetry, and numerical tests show that the DLWFs with an occupation of 1 are real. However, we observe substantial imaginary character in DLWFs that have an occupation numerically distinguishable from 1. Even though the arguments in [22] do not differentiate between the occupied and unoccupied spaces, we conjecture that they do not apply to Wannier functions whose occupation is far from 1. It is possible, however, that the imaginary character of fractionally occupied DLWFs is because F lacks a unique global minimum.

V. ACKNOWLEDGEMENTS

We acknowledge support from the National Science Foundation (Grant No. CHE-2154831). A.M. was additionally supported by the Molecular Sciences Software Institute Phase-II Software Fellowship, and J.Z.W. by the National Institutes of Health (Grant No. 5R01GM061870).

-
- [1] N. W. Ashcroft and N. D. Mermin, *Solid-State Physics*, 1st ed. (Harcourt, Orlando, FL, 1976).
 - [2] G. H. Wannier, Phys. Rev. **52**, 191 (1937).
 - [3] P. L. Silvestrelli and M. Parrinello, Phys. Rev. Lett. **82**, 3308 (1999).
 - [4] P. L. Silvestrelli and M. Parrinello, Phys. Rev. Lett. **82**, 5415 (1999).
 - [5] P. L. Silvestrelli and M. Parrinello, The Journal of Chemical Physics **111**, 3572 (1999).
 - [6] Y.-S. Lee, M. B. Nardelli, and N. Marzari, Phys. Rev. Lett. **95**, 076804 (2005).
 - [7] E. Y. Li and N. Marzari, ACS Nano **5**, 9726 (2011).
 - [8] M. Shelley, N. Poilvert, A. A. Mostofi, and N. Marzari, Computer Physics Communications **182**, 2174 (2011).
 - [9] S. Goedecker, Rev. Mod. Phys. **71**, 1085 (1999).
 - [10] I. Souza, N. Marzari, and D. Vanderbilt, Phys. Rev. B **65**, 035109 (2001).
 - [11] N. Marzari and D. Vanderbilt, Phys. Rev. B **56**, 12847 (1997).
 - [12] R. Resta, *Berry's Phase and Geometric Quantum Distance. Macroscopic Polarization and Electron Localization*, Troisième Cycle de La Physique En Suisse Romande (EPFL, Lausanne, Lausanne, 2000).
 - [13] M. Stengel and N. A. Spaldin, Phys. Rev. B **77**, 155106 (2008).
 - [14] G. Borghi, A. Ferretti, N. L. Nguyen, I. Dabo, and N. Marzari, Phys. Rev. B **90**, 075135 (2014).
 - [15] J. Ma and L.-W. Wang, Sci. Rep. **6**, 24924 (2016).
 - [16] D. Wing, G. Ohad, J. B. Haber, M. R. Filip, S. E. Gant, J. B. Neaton, and L. Kronik, Proc Natl Acad Sci USA **118**, e2104556118 (2021).
 - [17] H. J. Monkhorst and J. D. Pack, Phys. Rev. B **13**, 5188 (1976).
 - [18] J. des Cloizeaux, Phys. Rev. **135**, A685 (1964).
 - [19] J. des Cloizeaux, Phys. Rev. **129**, 554 (1963).
 - [20] J. M. Foster and S. F. Boys, Rev. Mod. Phys. **32**, 300 (1960).
 - [21] W. Kohn, Phys. Rev. **115**, 809 (1959).
 - [22] C. Brouder, G. Panati, M. Calandra, C. Mourougane, and N. Marzari, Phys. Rev. Lett. **98**, 046402 (2007).
 - [23] G. Panati and A. Pisante, Commun. Math. Phys. **322**, 835 (2013).
 - [24] F. Gygi, J.-L. Fattebert, and E. Schwegler, Computer Physics Communications **155**, 1 (2003).
 - [25] F. Giustino and A. Pasquarello, Phys. Rev. Lett. **96**, 216403 (2006).
 - [26] N. Q. Su, A. Mahler, and W. Yang, J. Phys. Chem. Lett. **11**, 1528 (2020).
 - [27] C. Li, X. Zheng, N. Q. Su, and W. Yang, Nat. Sci. Rev. **5**, 203 (2018).
 - [28] I. Daubechies, *Ten Lectures on Wavelets*, CBMS-NSF Regional Conference Series in Applied Mathematics No. 61 (Society for Industrial and Applied Mathematics, 1992).
 - [29] R. Dawes and T. Carrington, Jr., The Journal of Chemical Physics **124**, 054102 (2006).
 - [30] J. E. Subotnik, R. J. Cave, R. P. Steele, and N. Shenvi, The Journal of Chemical Physics **130**, 234102 (2009).
 - [31] A. A. Mostofi, J. R. Yates, Y.-S. Lee, I. Souza, D. Vanderbilt, and N. Marzari, Computer Physics Communications **178**, 685 (2008).
 - [32] A. A. Mostofi, J. R. Yates, G. Pizzi, Y.-S. Lee, I. Souza, D. Vanderbilt, and N. Marzari, Computer Physics Communications **185**, 2309 (2014).
 - [33] G. Pizzi, V. Vitale, R. Arita, S. Blügel, F. Freimuth, G. Géranton, M. Gibertini, D. Gresch, C. Johnson, T. Koretsune, J. Ibañez-Azpiroz, H. Lee, J.-M. Lihm, D. Marchand, A. Marrazzo, Y. Mokrousov, J. I. Mustafa,

- Y. Nohara, Y. Nomura, L. Paulatto, S. Poncé, T. Ponweiser, J. Qiao, F. Thöle, S. S. Tsirkin, M. Wierzbowska, N. Marzari, D. Vanderbilt, I. Souza, A. A. Mostofi, and J. R. Yates, *J. Phys.: Condens. Matter* **32**, 165902 (2020).
- [34] E. Polak and G. Ribiere, *R.I.R.O.* **3**, 35 (1969).
- [35] R. Fletcher and C. M. Reeves, *The Computer Journal* **7**, 149 (1964).
- [36] W. H. Press, S. A. Teukolsky, W. T. Vetterling, and B. P. Flannery, *Numerical Recipes in FORTRAN: The Art of Scientific Computing*, 2nd ed., Fortran Numerical Recipes, Vol. 1 (Cambridge University Press, The Pitt Building, Trumpington Street, Cambridge CB2 1RP, 1992).
- [37] A. Mahler, `Mtesseracted/wannier90: CostSE`, <https://github.com/mtesseracted/wannier90> (2024).
- [38] J. P. Perdew, K. Burke, and M. Ernzerhof, *Phys. Rev. Lett.* **77**, 3865 (1996).
- [39] D. R. Hamann, *Phys. Rev. B* **88**, 085117 (2013).
- [40] M. J. van Setten, M. Giantomassi, E. Bousquet, M. J. Verstraete, D. R. Hamann, X. Gonze, and G. M. Rignanese, *Computer Physics Communications* **226**, 39 (2018).
- [41] P. Giannozzi, S. Baroni, N. Bonini, M. Calandra, R. Car, C. Cavazzoni, D. Ceresoli, G. L. Chiarotti, M. Cococcioni, I. Dabo, A. Dal Corso, S. de Gironcoli, S. Fabris, G. Fratesi, R. Gebauer, U. Gerstmann, C. Gougoussis, A. Kokalj, M. Lazzeri, L. Martin-Samos, N. Marzari, F. Mauri, R. Mazzarello, S. Paolini, A. Pasquarello, L. Paulatto, C. Sbraccia, S. Scandolo, G. Sclauzero, A. P. Seitsonen, A. Smogunov, P. Umari, and R. M. Wentzcovitch, *J. Phys.: Condens. Matter* **21**, 395502 (2009).
- [42] P. Giannozzi, O. Andreussi, T. Brumme, O. Bunau, M. Buongiorno Nardelli, M. Calandra, R. Car, C. Cavazzoni, D. Ceresoli, M. Cococcioni, N. Colonna, I. Carnimeo, A. Dal Corso, S. de Gironcoli, P. Delugas, R. A. DiStasio, A. Ferretti, A. Floris, G. Fratesi, G. Fugallo, R. Gebauer, U. Gerstmann, F. Giustino, T. Gorni, J. Jia, M. Kawamura, H.-Y. Ko, A. Kokalj, E. Küçükbenli, M. Lazzeri, M. Marsili, N. Marzari, F. Mauri, N. L. Nguyen, H.-V. Nguyen, A. Otero-de-la-Roza, L. Paulatto, S. Poncé, D. Rocca, R. Sabatini, B. Santra, M. Schlipf, A. P. Seitsonen, A. Smogunov, I. Timrov, T. Thonhauser, P. Umari, N. Vast, X. Wu, and S. Baroni, *J. Phys.: Condens. Matter* **29**, 465901 (2017).
- [43] T. Hom, W. Kiszenik, and B. Post, *J Appl Cryst* **8**, 457 (1975).
- [44] O. J. Rutt, G. R. Williams, and S. J. Clarke, *Chem. Commun.*, 2869 (2006).
- [45] W. Kohn, *Phys. Rev. B* **7**, 4388 (1973).
- [46] J. P. Perdew, R. G. Parr, M. Levy, and J. L. Balduz, *Phys. Rev. Lett.* **49**, 1691 (1982).
- [47] A. Damle and L. Lin, *Multiscale Model. Simul.* **16**, 1392 (2018).
- [48] A. Damle, L. Lin, and L. Ying, *J. Chem. Theory Comput.* **11**, 1463 (2015).
- [49] A. Damle, L. Lin, and L. Ying, *Journal of Computational Physics* **334**, 1 (2017).

Supplemental Material for Wannier Functions Dually Localized in Space and Energy

Aaron Mahler

Duke University, Department of Physics, Durham, NC 27708

Jacob Z. Williams

Duke University, Department of Chemistry, Durham, NC 27708

Neil Qiang Su

*Department of Chemistry, Key Laboratory of Advanced Energy Materials Chemistry
(Ministry of Education) and Renewable Energy Conversion and Storage Center (RECAST),*

Nankai University, Tianjin 300071, China and

Duke University, Department of Chemistry, Durham, NC 27708

Weitao Yang*

Duke University, Department of Chemistry, Durham, NC 27708 and

Duke University, Department of Physics, Durham, NC 27708

(Dated: August 20, 2024)

I. GAUGE-INVARIANT ENERGY COST WITH DISENTANGLEMENT

The projector \tilde{P} onto the subspace spanned by the disentangled bands $|\tilde{\psi}_{\mathbf{k}i}\rangle$ can be written in either the disentangled Bloch or Wannier basis:

$$\tilde{P} = \sum_{\mathbf{k}i} |\tilde{\psi}_{\mathbf{k}i}\rangle \langle \tilde{\psi}_{\mathbf{k}i}| = \sum_{\mathbf{R}i} |w_{\mathbf{R}i}\rangle \langle w_{\mathbf{R}i}|. \quad (1)$$

Then we can write the gauge-invariant part of the energy cost Ξ as

$$\begin{aligned} \Xi_{\text{I}} &= \sum_i \left[\langle w_{\mathbf{0}i} | \tilde{h}^2 | w_{\mathbf{0}i} \rangle - \sum_{\mathbf{R}j} |\langle w_{\mathbf{R}j} | \tilde{h} | w_{\mathbf{0}i} \rangle|^2 \right] \\ &= \sum_i \left[\langle w_{\mathbf{0}i} | \tilde{h}^2 | w_{\mathbf{0}i} \rangle - \sum_{\mathbf{R}j} \langle w_{\mathbf{0}i} | \tilde{h} | w_{\mathbf{R}j} \rangle \langle w_{\mathbf{R}j} | \tilde{h} | w_{\mathbf{0}i} \rangle \right] \\ &= \sum_i \left[\langle w_{\mathbf{0}i} | \tilde{h}^2 | w_{\mathbf{0}i} \rangle - \langle w_{\mathbf{0}i} | \tilde{h} \left(\sum_{\mathbf{R}j} |w_{\mathbf{R}j}\rangle \langle w_{\mathbf{R}j}| \right) \tilde{h} | w_{\mathbf{0}i} \rangle \right] \\ &= \sum_i \left[\langle w_{\mathbf{0}i} | \tilde{h}^2 | w_{\mathbf{0}i} \rangle - \langle w_{\mathbf{0}i} | \tilde{h} \tilde{P} \tilde{h} | w_{\mathbf{0}i} \rangle \right] = \sum_i \langle w_{\mathbf{0}i} | \tilde{h} \tilde{I} \tilde{h} - \tilde{h} \tilde{P} \tilde{h} | w_{\mathbf{0}i} \rangle \\ &= \sum_i \langle w_{\mathbf{0}i} | \tilde{h}^2 | w_{\mathbf{0}i} \rangle - \sum_i \langle w_{\mathbf{0}i} | \tilde{h} \tilde{P} \tilde{h} | w_{\mathbf{0}i} \rangle = \\ &= \text{Tr}_c [\tilde{P} \tilde{h}^2] - \text{Tr}_c [\tilde{P} \tilde{h} \tilde{P} \tilde{h}]. \end{aligned} \quad (2)$$

Noting that

$$\begin{aligned} \tilde{P} \tilde{h} &= \left(\sum_{\mathbf{k}i} |\tilde{\psi}_{\mathbf{k}i}\rangle \langle \tilde{\psi}_{\mathbf{k}i}| \right) \left(\sum_{\mathbf{k}'i'} \tilde{\varepsilon}_{\mathbf{k}'i'} |\tilde{\psi}_{\mathbf{k}'i'}\rangle \langle \tilde{\psi}_{\mathbf{k}'i'}| \right) \\ &= \sum_{\mathbf{k}\mathbf{k}'i'i'} \tilde{\varepsilon}_{\mathbf{k}'i'} |\tilde{\psi}_{\mathbf{k}i}\rangle \langle \tilde{\psi}_{\mathbf{k}i}| \tilde{\psi}_{\mathbf{k}'i'} \rangle \langle \tilde{\psi}_{\mathbf{k}'i'}| \\ &= \sum_{\mathbf{k}i} \tilde{\varepsilon}_{\mathbf{k}i} |\tilde{\psi}_{\mathbf{k}i}\rangle \langle \tilde{\psi}_{\mathbf{k}i}| \\ &= \tilde{h}, \end{aligned} \quad (3)$$

whence $\tilde{P} \tilde{h}^2 = \tilde{P} \tilde{h} \tilde{P} \tilde{h} = \tilde{h}^2$, we obtain that

$$\Xi_{\text{I}} = \text{Tr}_c [\tilde{P} \tilde{h}^2] - \text{Tr}_c [\tilde{P} \tilde{h} \tilde{P} \tilde{h}] = 0. \quad (4)$$

II. APPENDIX OF TABLES

This section shows the spatial center ($\langle r_x \rangle, \langle r_y \rangle, \langle r_z \rangle$), spatial variance $\langle \Delta r^2 \rangle$, average energy $\langle h \rangle$, energy variance $\langle \Delta h^2 \rangle$, and occupation $\lambda_{\mathbf{0}ii} = \langle w_{\mathbf{0}i} | \rho | w_{\mathbf{0}i} \rangle$ of the individual

* weitao.yang@duke.edu

DLWFs presented in the Results section of the main text. The index is ordered from lowest to highest energy, starting at 1. Thus, the index in Table III (Table IV, Table V) below corresponds to the DLWF density isoplot labels in Fig. 4 (Fig. 5, Fig. 6) of the main text.

A. Silicon

TABLE I: Spatial and energy information per DLWF when only using the valence states of silicon.

index	$\langle r_x \rangle$	$\langle r_y \rangle$	$\langle r_z \rangle$	$\langle \Delta r^2 \rangle$	$\langle h \rangle$	$\langle \Delta h^2 \rangle$	$\lambda_{\mathbf{0}ii}$
1	0.6280	0.7208	0.7298	2.346988	-3.228980	1.700047	1.000000
2	-1.1404	-0.8386	-0.2173	4.867715	0.533916	3.614710	1.000000
3	0.9968	0.0737	1.6037	4.481121	3.718522	1.627641	1.000000
4	-0.2461	0.0736	0.3609	4.481166	3.718535	1.627611	1.000000

TABLE II: Spatial and energy information per DLWF when using 12 bands disentangled to produce 8 DLWFs.

index	$\langle r_x \rangle$	$\langle r_y \rangle$	$\langle r_z \rangle$	$\langle \Delta r^2 \rangle$	$\langle h \rangle$	$\langle \Delta h^2 \rangle$	$\lambda_{\mathbf{0}ii}$
1	0.6393	0.7274	0.7274	2.358287	-3.234109	1.681093	0.999994
2	-0.5300	-0.2339	-0.2340	4.840094	0.528172	3.587587	0.999599
3	-1.4288	-1.1217	0.3475	4.369317	3.733272	1.664589	0.998669
4	1.2869	0.3475	1.5940	4.369209	3.733309	1.664698	0.998666
5	0.0548	0.0466	0.0468	3.821754	11.392893	4.591103	0.000972
6	-0.0529	1.4009	1.4007	3.817564	11.396780	4.589852	0.000944
7	-1.3560	-0.0132	4.0654	3.822250	11.428582	4.551941	0.000580
8	-1.3552	1.3505	2.7017	3.819881	11.430745	4.553351	0.000577

TABLE III: Spatial and energy information per DLWF for silicon using 34 bands disentangled to 30 bands.

index	$\langle r_x \rangle$	$\langle r_y \rangle$	$\langle r_z \rangle$	$\langle \Delta r^2 \rangle$	$\langle h \rangle$	$\langle \Delta h^2 \rangle$	$\lambda_{\mathbf{0}ii}$
-------	-----------------------	-----------------------	-----------------------	------------------------------	---------------------	------------------------------	--------------------------

1	-0.7273	-0.6394	-0.7274	2.357579	-3.234141	1.681126	0.999992
2	0.2355	0.5311	0.2360	4.824702	0.528461	3.594108	0.999453
3	-0.3476	-1.2893	-1.5917	4.296241	3.738779	1.693098	0.997848
4	-1.5941	-1.2878	-0.3466	4.294985	3.738866	1.692406	0.997860
5	-0.0505	2.6608	2.7073	4.845865	10.548782	4.084945	0.001534
6	1.2678	0.0730	1.2995	4.853594	10.569209	4.085532	0.001481
7	1.4140	-1.3094	-2.7687	4.916316	10.693759	4.064643	0.000875
8	0.0238	1.3053	1.3575	4.907699	10.711160	4.088860	0.000869
9	-0.0182	0.0123	0.0392	8.239568	15.653925	3.218761	0.000047
10	-0.8270	-0.8582	-1.3807	8.298693	15.739891	2.969253	0.000037
11	0.1125	-1.2840	-1.3794	8.389856	18.404274	1.924312	0.000001
12	-0.7443	-0.7126	0.0674	8.252689	18.922132	1.841812	0.000002
13	1.0858	-0.0787	1.4867	8.336248	19.346286	2.670695	0.000001
14	-0.1180	-1.1155	1.2004	9.336795	21.777131	3.725877	0.000000
15	0.0191	-1.2920	-1.3532	8.073594	25.390255	2.437707	0.000000
16	0.0175	0.0323	-0.0157	8.196600	25.395202	2.166016	0.000000
17	1.3469	0.2140	1.1390	8.188723	25.429163	2.396005	0.000000
18	-1.4098	0.0256	-1.3264	7.304936	25.916725	3.080916	0.000000
19	1.3965	0.0338	-1.3458	9.008920	26.269281	2.215705	0.000000
20	0.3826	0.3316	0.4795	10.802935	29.338486	3.072971	0.000000
21	-0.0229	-2.7464	-2.7040	8.376918	31.775110	3.252854	0.000000
22	-1.3644	-2.7038	1.3521	8.258431	31.791921	3.342923	0.000000
23	-0.0453	-1.3281	-1.3151	8.891537	32.291000	2.209553	0.000000
24	-0.0594	-1.3083	1.3658	9.803869	34.805345	3.125115	0.000000
25	1.1648	-1.2274	0.1947	9.635747	35.629707	3.195436	0.000000
26	-2.6160	-0.0473	0.0126	9.687295	35.795476	3.419050	0.000000
27	2.5350	-0.1019	-2.5121	9.086322	37.532297	3.298730	0.000000
28	1.3284	-0.0261	-1.3222	8.512641	39.136116	3.739278	0.000000
29	0.0396	2.7316	-0.0278	9.142814	39.527945	3.099532	0.000000
30	0.0056	1.3209	1.3000	9.366045	40.314612	2.403746	0.000000

B. Copper

TABLE IV. Spatial and energy information per DLWF for copper.

index	$\langle r_x \rangle$	$\langle r_y \rangle$	$\langle r_z \rangle$	$\langle \Delta r^2 \rangle$	$\langle h \rangle$	$\langle \Delta h^2 \rangle$	λ_{0ii}
01	-0.0000	0.0000	-0.0000	0.155525	-95.528687	0.000018	1.000000
02	0.0000	0.0000	0.0000	0.186959	-52.928957	0.000814	1.000000
03	0.0000	-0.0000	0.0000	0.186943	-52.928955	0.000811	1.000000
04	-0.0000	-0.0000	-0.0000	0.186958	-52.928954	0.000811	1.000000
05	-0.1631	-0.0051	0.0045	1.326589	13.553628	3.061090	0.996669
06	-0.0038	-0.0046	-0.0073	0.705379	14.072693	1.235276	0.996415
07	-0.0063	0.0014	-0.0177	0.793226	14.078952	1.528006	0.996099
08	-0.0068	-0.0050	0.0046	0.709318	14.085334	1.248489	0.996337
09	0.0096	0.0045	-0.0013	0.803549	14.121215	1.528358	0.996831
10	1.0363	0.9041	-0.8420	4.926801	16.988522	7.848977	0.516482
11	0.6418	-1.0563	-0.3213	7.008280	26.141562	16.535585	0.000001
12	-0.4665	-0.0404	1.4063	7.196124	32.475400	19.176457	0.000000
13	-0.4218	1.0018	1.0964	7.318156	32.739401	20.308781	0.000000
14	0.0123	0.0419	-0.0969	12.324220	39.582046	8.504523	0.000000
15	1.1162	-0.7577	-1.2117	13.706412	45.246294	12.532017	0.001148
16	1.1295	-1.5696	-1.3568	11.206204	51.485678	15.577288	0.000009
17	1.1818	-0.9269	0.0903	8.954952	55.296748	12.405831	0.000009

C. Ethylene

TABLE V: Spatial and energy information per DLWF for ethylene, truncated to the lowest 20 states.

index	$\langle r_x \rangle$	$\langle r_y \rangle$	$\langle r_z \rangle$	$\langle \Delta r^2 \rangle$	$\langle h \rangle$	$\langle \Delta h^2 \rangle$	λ_{0ii}
1	-0.0000	-0.0000	0.0000	0.983945	-18.612524	0.000174	1.000000
2	0.0001	0.0000	0.0000	1.784198	-13.889465	0.000596	0.999997
3	0.0002	-0.0000	-0.0001	1.633431	-11.218850	0.003959	0.999974
4	-0.0004	0.0000	0.0000	1.497676	-9.940055	0.005812	0.999947
5	-0.0010	-0.0000	-0.0000	2.015195	-8.185370	0.007015	0.999939
6	0.0000	0.0000	-0.0002	1.329210	-6.559715	0.010217	0.999856
7	0.0007	0.0000	0.0014	2.009921	-0.717311	0.135739	0.000000
8	-1.1695	2.1974	-0.1999	3.337830	1.292702	1.286921	0.000025
9	-1.1696	-2.1974	-0.2001	3.337846	1.292738	1.286973	0.000025
10	2.2760	-1.8212	-0.0673	3.315293	1.349986	1.214562	0.000036
11	2.2761	1.8212	-0.0673	3.315328	1.350045	1.214551	0.000036
12	-3.3293	0.0001	-0.0157	3.786638	1.493888	1.128354	0.000011
13	-0.0724	0.0004	-2.7003	3.546867	1.955814	1.377605	0.000052
14	-0.0642	1.5299	2.4554	4.019978	2.136463	1.134380	0.000044
15	-0.0651	-1.5302	2.4552	4.020222	2.136698	1.134326	0.000044
16	-0.1124	3.2622	-3.9195	4.562633	2.820583	1.205123	0.000002
17	-0.1124	-3.2610	-3.9198	4.562800	2.820617	1.205088	0.000002
18	-4.4466	-3.2543	-0.1016	4.613289	2.977994	1.161815	0.000002
19	-4.4465	3.2544	-0.1015	4.613393	2.978025	1.161790	0.000002
20	-3.4117	4.9992	3.3338	4.192816	2.989893	1.415940	0.000000

III. BAND STRUCTURES

Here we show the disentangled band structures used for the systems reported in the main text. Observe that the disentangled band structure agrees almost exactly with the full band structure near the Fermi energy. We found that DLWFs with a mixing parameter of $\gamma = 0.01$ gave the best interpolation, which was slightly better than using $\gamma = 0.0$ (MLWF) and noticeably better than the value of $\gamma = 0.47714$ used in the isosurface plots. See Supplemental Sec. III A for details.

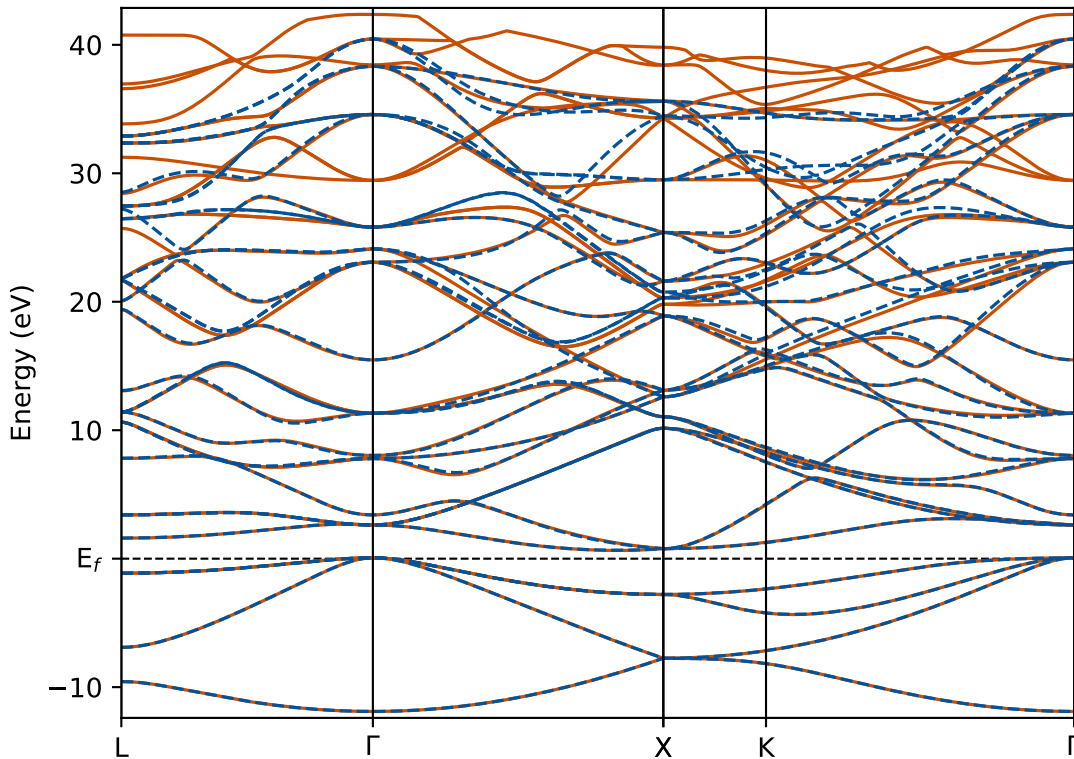


FIG. 1. Disentangled band structure of silicon used for the isosurface plots in the main text. The solid orange lines are 34 bands from a non-self-consistent calculation in `Quantum ESPRESSO` with the zero point of the y -axis set at the Fermi energy. The dashed blue lines are 30 disentangled bands interpolated along the path through the Brillouin zone using DLWFs with a mixing parameter of $\gamma = 0.01$.

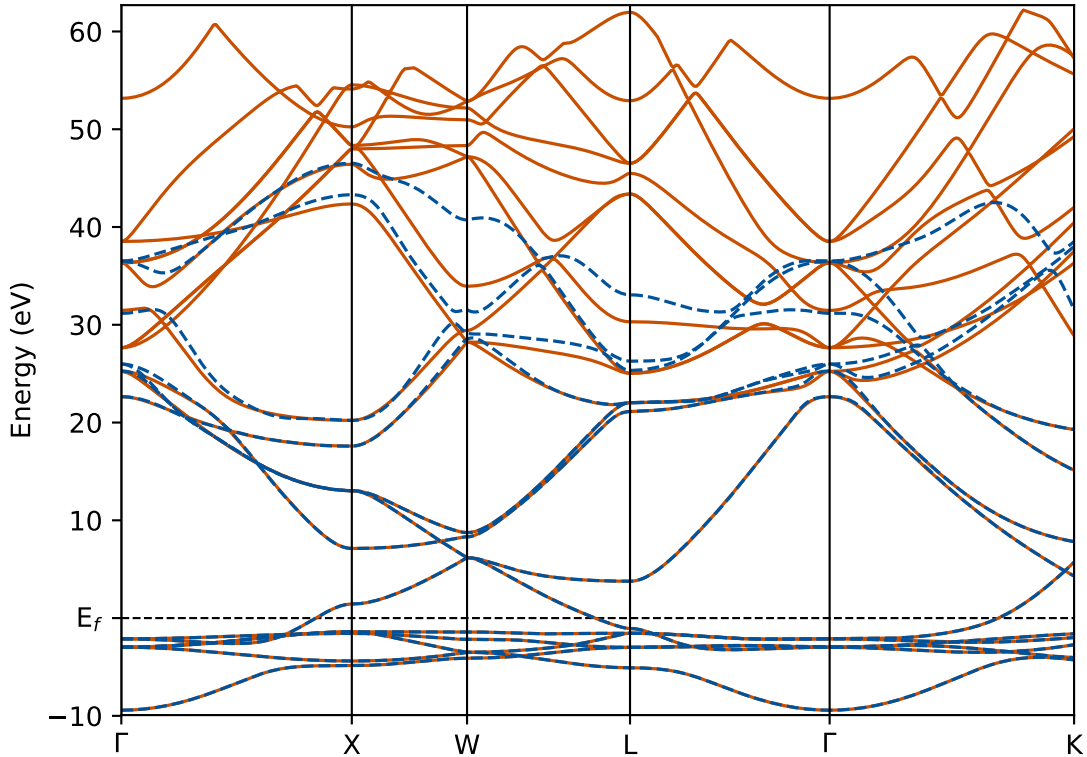


FIG. 2. Disentangled band structure of copper used for the isosurface plots in the main text. The solid orange lines are 23 bands from a non-SCF calculation in `Quantum ESPRESSO`, and the energy axis is zeroed at the Fermi energy. The dashed blue lines are 17 disentangled bands interpolated along the path through the Brillouin zone using DLWFs with a mixing parameter of $\gamma = 0.01$.

A. Interpolated Band Structure Errors in Silicon

Here we show some interpolated band structure plots for specific values of γ in the case of silicon. The plots shown in Figs. 3a–3f are for 12 bands disentangled to produce 8 Wannier functions, the average interpolation error which is reported in the main text. For the case of 34 bands disentangled down to 30, the average squared error for the band interpolation along the path in Figs. 4a–4e is (a) 0.192989, (b) 0.176692, (c) 0.271211, (d) 0.411963, and (e) 0.695313 eV². Since the case of $\gamma = 0.01$ is slightly better than the MLWF case of $\gamma = 0.0$ we use this value for the band structure shown in the main text and previous section.

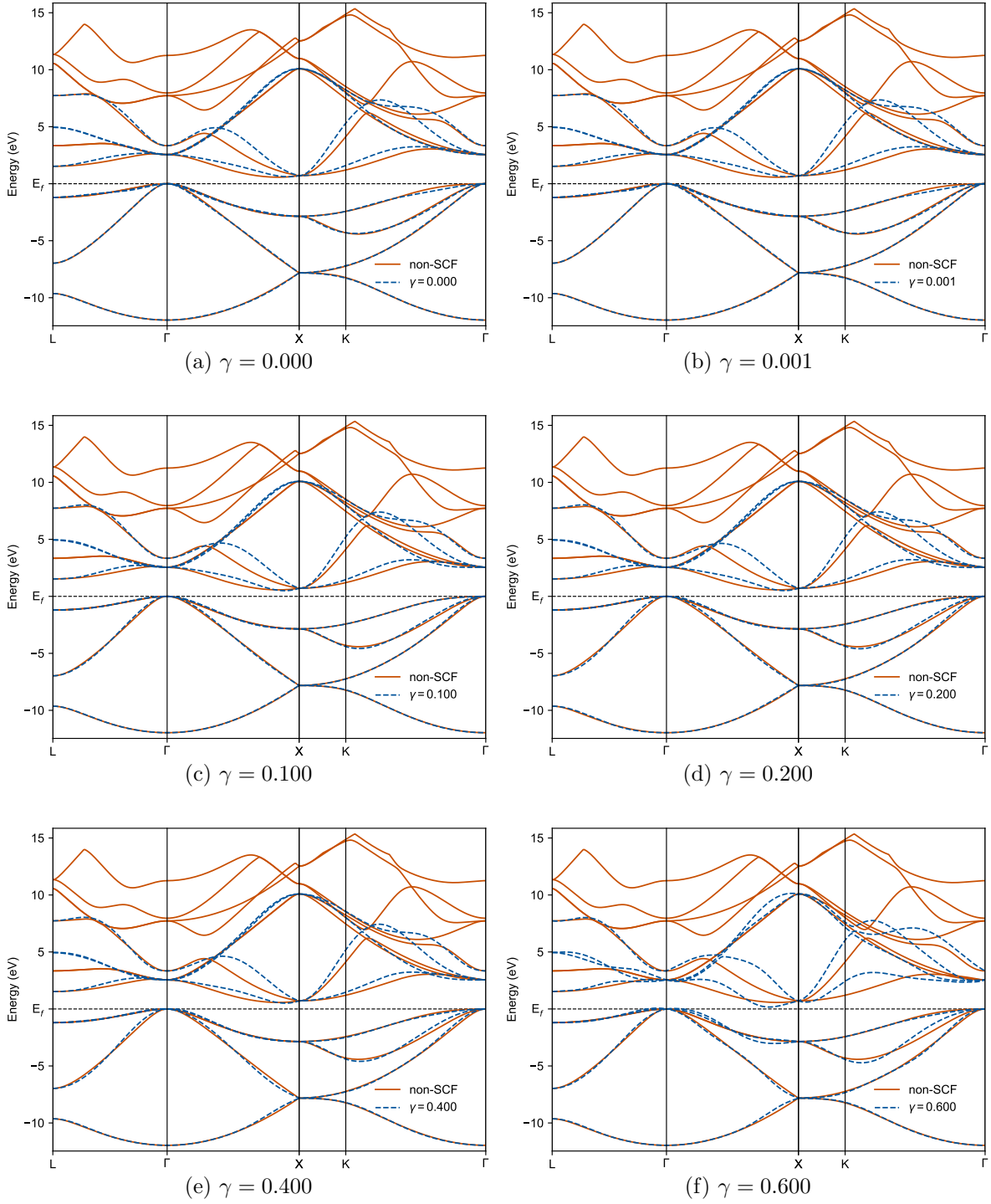


FIG. 3. Interpolated band structures for the frontier states of silicon (12 bands and 8 Wannier functions) for varying values of γ .

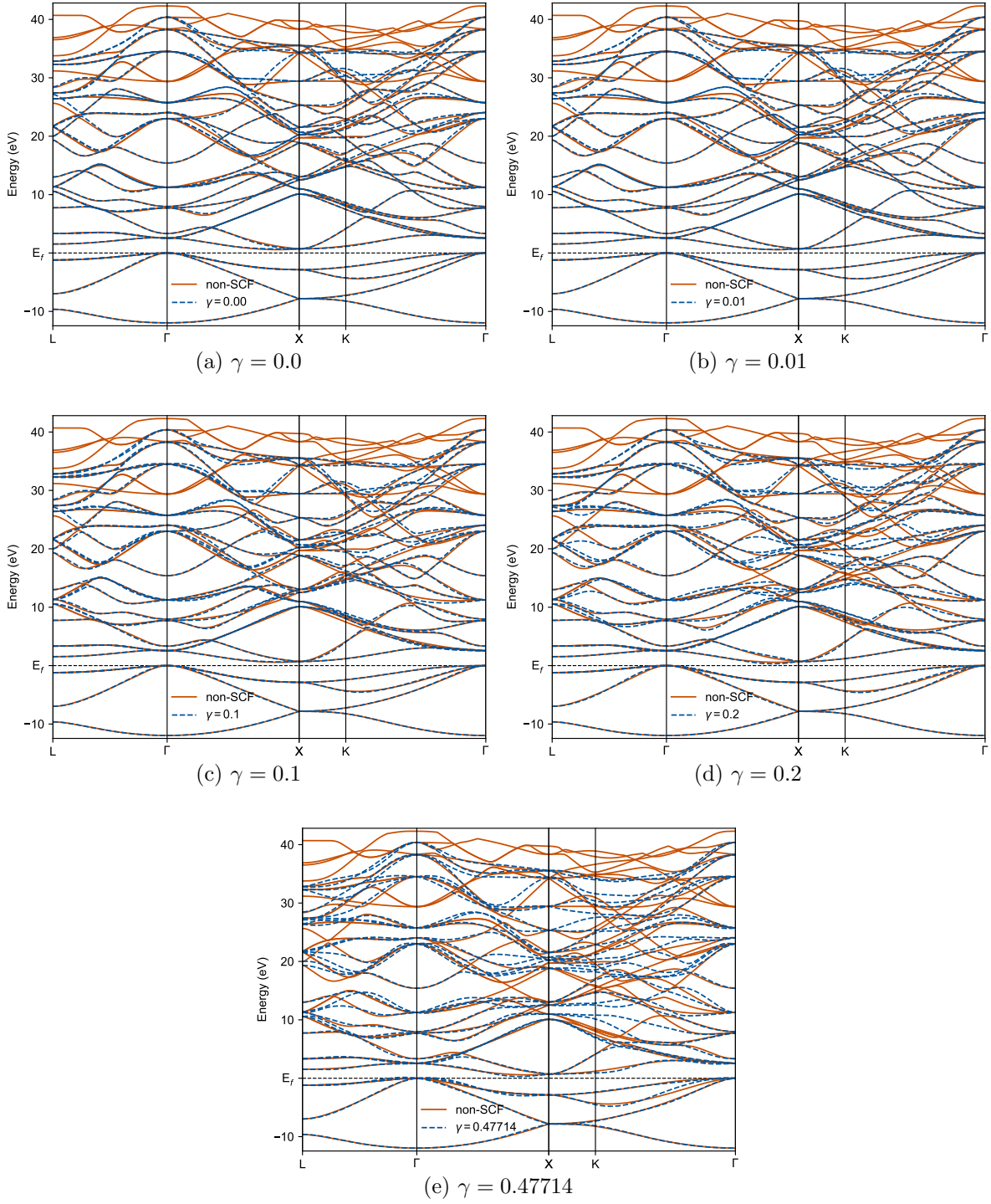


FIG. 4. Interpolated band structures for the converged states of silicon (34 bands and 30 Wannier functions) for varying values of γ .

IV. MIXING PARAMETER CONVERSION

In the molecular formulation of the localized orbital scaling correction (LOSC) method [1], the cost function is given as

$$F = (1 - \gamma')\Omega + \gamma'C'\Xi, \quad (5)$$

where Ω is the spatial variance cost and Ξ is the energy variance cost. We write γ' to differentiate from the mixing parameter γ used in the main text. The constant C' is added because in atomic units there is a large order of magnitude difference between typical space and energy spreads. This results in mixing parameters that are very close to 1.0, which are difficult to optimize. To keep the space and energy cost within the same order of magnitude, the factor of C was set to $1000 \text{ eV}^2/\text{a}_0^2$ (where a_0 is the Bohr radius). The implementation in `wannier90` uses the units of \AA and eV, which results in spreads that are of the same order of magnitude; thus, we use a factor of $C = 1(\text{eV}/\text{\AA})^2$ in that implementation of the cost function but do not include the symbol for brevity. Converting between these two different equations and units can be accomplished with the following formulae. When converting from Eq. (5), the equivalent mixing parameter for the cost function in the main text is given by

$$\gamma = \left(1 + \left(\frac{1 - \gamma'}{\gamma'} \right) m^2 C' \right)^{-1} \quad (6)$$

where $m = 0.529177210903/27.211386245988$ is the conversion from Bohr to \AA divided by the conversion from Hartree to eV. Values are obtained from the NIST CODATA database [2]. The conversion from the mixing parameter in the main text to the cost function in Eq. (5) is given by

$$\gamma' = \left(1 + \left(\frac{1 - \gamma}{\gamma m^2 C'} \right) \right)^{-1}. \quad (7)$$

V. CODE IMPLEMENTATION DETAILS

The cost function outlined in the main text was implemented in the `wannier90` code [3–5]. To implement the energy localization, the data structures necessary for energy localization are only calculated if energy localization is requested. The energy spread cost is calculated in the function `wann_xi`, which is called right after the function `wann_omega`,

which calculates the spatial spread. Similarly, the energy gradient is only calculated when needed and is calculated in `wann_dxi`, which is called right after the function that calculates the spatial spread gradient, `wann_domega`. The analytic gradient implemented in `wann_xi` was verified numerically for some test systems to ensure the derivation is correct. The additional data structures that hold the pertinent information for energy localization are `have` for average energy, `have2` for average energy squared, and `h2ave` for average of the squared energy. These variables are used to update the public variables `wannier_energies` and `wannier_espreads`, which are the energy version of the public variables `wannier_centres` and `wannier_spreads` used for spatial information. Since adding these variables into the library mode would necessitate a change to the API, this change was not implemented. If desired, these variables could be added to the API as optional arguments, which should prevent breaking any existing code that uses the API. Our modified code is hosted on GitHub at [6].

A. Keyword List

The `wannier90` program uses an input file named `seedname.win`, where `seedname` can be set from the command line. This input file contains key-value pairs in a free-form structure that controls the settings of the program. This is a list of the new keywords added in the implementation of energy localization in the `wannier90` code.

Keyword	Type	Description
Energy Mixing Parameters		
SP_EN_MIX	R	Space and energy mixing parameter
ECONV_MAX	R	Energy convergence maximum
NCNV_MAX	I	Number of WFs to use for convergence
NUM_OCC	I	Bloch orbital occupation per k-point
WRITE_INFO	L	Write localization information per WF to file
WANNIER_PLOT_DENSITY	L	Plot the WF density

TABLE VI: `seedname.win` file keywords controlling the energy localization. Argument types are represented by, I for a integer, R for a real number, and L for a logical value.

B. Keyword Details

`real :: sp_en_mix`

Space and energy mixing parameter; a value of 0.0 gives the MLWF cost function. This value must obey the inequality $0.0 \leq \text{sp_en_mix} \leq 1.0$. When $0.0 < \text{sp_en_mix}$ then the per WF information printed at every print cycle will change to include the energy statistics.

The default value is 0.0.

`real :: econv_max`

The upper bound for the energy window used for testing localization convergence. This is useful when considering high-energy unoccupied orbitals since they can be very noisy during the descent. If `econv_max` is set then an additional line will be printed at the end of each print cycle showing the spatial, energy, and total cost of the subset used for convergence. This setting cannot be set if `nconv_max` is set.

No default.

`integer :: nconv_max`

The number of Wannier functions used to test for convergence during the gradient descent in the Wannierisation procedure. Useful for when considering high-energy unoccupied orbitals since they can be too noisy to converge during the descent. If `nconv_max` is set then an additional line will be printed at the end of each print cycle showing the spatial, energy, and total cost of the subset used for convergence. This setting cannot be set if `econv_max` is set.

No default, but if `nconv_max > num_wann` it will be set to `num_wann`.

`integer :: num_occ`

The number of occupied of Bloch orbitals. This is used to print the occupation of the WFs. Since it is only a single integer this implementation only applies correctly for insulators and Γ -point calculations. In the typical case of finding MLWFs for occupied only orbitals the WF occupations will always be 1.0. Setting `num_occ` is useful when considering WFs that include both occupied and unoccupied Bloch orbitals.

No default.

`logical :: write_info`

If `true`, write a summary of the cost information per WF to the file `seedname.info` for the WFs in the home unit cell. The format is WF index, Cartesian expectation of center in \AA , spatial spread in \AA^2 . If `sp_en_mix` $\neq 0.0$ then it will additionally print the WF energy expectation in eV and the energy spread in eV^2 . If `num_occ` $\neq 0$ then it will also print the WF occupations.

The default value is `false`.

`logical :: wannier_plot_density`

Plot the WF density instead of the wavefunction, where the density is defined as $|w_n(\mathbf{r})|^2$. In the case of WFs that are not strictly real-valued, plotting the wavefunction will truncate the imaginary part. Plotting the density instead guarantees the whole WF is plotted.

The default value is `false`.

-
- [1] N. Q. Su, A. Mahler, and W. Yang, *J. Phys. Chem. Lett.* **11**, 1528 (2020).
- [2] E. Tiesinga, P. J. Mohr, D. B. Newell, and B. N. Taylor, The 2018 CODATA Recommended Values of the Fundamental Physical Constants, <https://physics.nist.gov/cuu/Constants/index.html> (2020).
- [3] A. A. Mostofi, J. R. Yates, Y.-S. Lee, I. Souza, D. Vanderbilt, and N. Marzari, *Computer Physics Communications* **178**, 685 (2008).

- [4] A. A. Mostofi, J. R. Yates, G. Pizzi, Y.-S. Lee, I. Souza, D. Vanderbilt, and N. Marzari, *Computer Physics Communications* **185**, 2309 (2014).
- [5] G. Pizzi, V. Vitale, R. Arita, S. Blügel, F. Freimuth, G. Géranton, M. Gibertini, D. Gresch, C. Johnson, T. Koretsune, J. Ibañez-Azpiroz, H. Lee, J.-M. Lihm, D. Marchand, A. Marrazzo, Y. Mokrousov, J. I. Mustafa, Y. Nohara, Y. Nomura, L. Paulatto, S. Poncé, T. Ponweiser, J. Qiao, F. Thöle, S. S. Tsirkin, M. Wierzbowska, N. Marzari, D. Vanderbilt, I. Souza, A. A. Mostofi, and J. R. Yates, *J. Phys.: Condens. Matter* **32**, 165902 (2020).
- [6] A. Mahler, Mtesseract/wannier90: CostSE, <https://github.com/mtesseract/wannier90> (2024).